Quantitative Analysis of DART Calibration Accuracy for Retrieving Spectral Signatures Over Urban Area

Zhijun Zhen, Jean-Philippe Gastellu-Etchegorry, Shengbo Chen, Tiangang Yin, Eric Chavanon, Nicolas Lauret, Jordan Guilleux

Quantitative Analysis of DART Calibration Accuracy for Retrieving Spectral Signatures Over Urban Area

Zhijun Zhen, Jean-Philippe Gastellu-Etchegorry, *Member, IEEE*, Shengbo Chen, *Member, IEEE*, Tiangang Yin, Eric Chavanon, Nicolas Lauret, and Jordan Guilleux

***Abstract*—Discrete anisotropic radiative transfer (DART) calibration is an iterative inversion method that is applied to shortwave (SW) satellite images to get maps of spectral signatures (SS) of city materials at the satellite spatial resolution. Therefore, it is potentially a handy spectral unmixing tool. However, up to now, it has only been validated by comparing the time series of SW radiative budget Q^*_{SW} from a flux tower in Basel to DART simulated Q^*_{SW} using maps of SS derived from satellite images. This article thoroughly assesses the DART calibration accuracy with two synthetic case studies, called "ideal" and "nonideal," for short wavelengths. In both cases, the satellite image is a DART simulated image of an urban scene with ground, buildings with various structures, water, and shrubs. In the ideal case, SS maps are the only unknowns in the inversion process. The mean absolute value of the relative errors over all bands for ground, roof, water, tree, and shrub maps were 0.013, 0.005, 0.027, 0.297, and 0.250. In the nonideal case, we considered an uncertainty on parameters assumed to be known in the ideal case: solar zenith angle (SZA); satellite image spatial resolution; pixel-shift; inaccuracy of landscape modeling; and modulation transfer function (MTF). It led to larger errors: for ground, roof, water, tree, and shrubs, the mean absolute value of the relative error was 0.233, 0.507, 3.088, 0.834, and 1.256, respectively. By descending order of importance, the parameters that most affect the accuracy of the retrieved SS of urban material were SZA, satellite image spatial resolution, pixel-shift, inaccuracy of three-dimensional urban scene modeling, and MTF.**

***Index Terms*—DART, reflectance, spectral confusion, spectral mixed model, urban meteorology.**

I. Introduction

SPACE-TIME variations of the spectral signatures (SSs) of city materials play an essential role in the energy balance models, characterization, and classification of urban material and surface changes [1]. They provide basic modeling parameters for many research works, such as climate change adaptation and sustainable human health development [2]. However, the current understanding of the separation of city materials and their spectral signatures is insufficient [3]. Indeed, it is challenging to determine SS since they vary with time and space. The roof is a typical example since its reflectance depends on its weathering state [4]. Therefore, it is necessary to consider the spatial and temporal changes of each urban material SS [5].

Remote sensing is a potentially ideal tool since it provides time-series satellite images of cities [6]. However, cities have very complex and various 3-D geometries [7]. The associated multiple-scattering events explain that the observed reflectance at the pixel level depends on the radiative interactions between the urban components present in the same pixel and between these components and neighbor urban components [8]. In short, the observed pixel reflectance is a complex function of the SS of urban components inside and outside that pixel. The complexity of the problem depends both on the spatial variability of the urban geometry and the spatial resolution of the remote sensing sensor. Therefore, the accurate retrieval of the SS of city material [9] is a complex mixed pixel problem, especially if several urban components are present in the pixel [10].

Mixed pixels are generally analyzed using either a linear spectral mixture analysis (LSMA) or nonlinear spectral mixture analysis [11]–[15]. LSMA is widely used for its simplicity because it ignores the multiple scattering among components within a pixel and assumes that the reflectance of each mixed pixel is a linear sum of the reflectance of the present components or endmembers weighted by the endmembers' abundance in each mixed pixel [16]–[18]. Decomposing mixed pixels into a number of endmembers SS requires approximating their proportion per pixel (fraction images). Several standard methods allow one to estimate fractional abundance, including the least squares [18], modified Gramm-Schmidt orthogonal decomposition [19], or singular value decomposition [20]. Model fit is sometimes evaluated using error metric root-mean-square error [21].

Early LSMA considers each endmember to have a unique spectrum, assuming that the number of endmembers combined with their spectral separability allows one to avoid confusion [22]. Consequently, it cannot treat the full spatial variation of urban SS in a given urban landscape. Depending on the spatial resolution of the satellite image and the specific 3-D urban

Manuscript received May 22, 2021; revised July 11, 2021; accepted August 30, 2021. Date of publication September 8, 2021; date of current version October 15, 2021. This work was supported in part by a TOSCA program of the French Space Center and in part by CSC. *(Corresponding authors: Jean-Philippe Gastellu-Etchegorry; Shengbo Chen.)*

Zhijun Zhen is with the Centre d'Etudes Spatiales de la Biosphere, University of Toulouse, 31062 Toulouse, France, and also with the College of Geoexploration Science and Technology, Jilin University, Changchun 130026, China (e-mail: zhenzj2312@mails.jlu.edu.cn).

Jean-Philippe Gastellu-Etchegorry, Eric Chavanon, Nicolas Lauret, and Jordan Guilleux are with the Centre d'Etudes Spatiales de la Biosphere, University of Toulouse, 31062 Toulouse, France (e-mail: jean-philippe.gastellu-etchegorry@cesbio.cnes.fr; eric.chavanon@cesbio.cnes.fr; nicolas.lauret@cesbio.cnes.fr; guilleuxj@cesbio.cnes.fr).

Shengbo Chen is with the College of Geoexploration Science and Technology, Jilin University, Changchun 130026, China (e-mail: chensb@jlu.edu.cn).

Tiangang Yin is with Earth System Science Interdisciplinary Center, University of Maryland, College Park, MD 20740-3823 USA (e-mail: tiangang.yin.85@gmail.com).

Digital Object Identifier 10.1109/JSTARS.2021.3110811

geometry and its numeric representation, two significant issues are encountered when applying LSMA to an urban environment: the multiple endmember problem in a class if the SS of this class varies [23], and the nonpure pixel problem if there are no pure pixels for urban materials [24].

Various methods have been devised to solve the above two problems separately. For example, multiple endmember spectral mixture analysis (MESMA) [23] and its derivation class-based MESMA [25], hierarchical MESMA [21], and stratified classification MESMA [26] are used to solve the multiple endmember problem. Their core concept is to classify distinct classes and then use MESMA to identify multiple endmembers within the classes and account for SS' temporal changes. Besides, minimum volume simplex analysis (MVSA) [24] addresses hyperspectral unmixing by applying a minimal volume simplex to the hyperspectral images, minimizing the same objective feature, and minimizing a regularized least-squares fit of the data restricting the abundance fractions that belong to the likelihood simplex to solve nonpure pixel problems. Two significant issues must be noted: MESMA needs various endmembers SS within each class. In addition, very high classification accuracy is required because the final accuracy depends heavily on the classification. However, misclassification is very difficult to avoid for materials that share similar SS. MVSA requires hyperspectral images, and the number of bands of satellite images must be at least larger than the number of endmembers. Moreover, due to the frequent interclass and intraclass spectral variability in urban areas, these two problems always exist together. In addition, recent work has shown that the vertical dimension has a significant impact on the functioning of the specific ecosystem [27], which stresses the interest in studying city landscapes from a 3-D perspective.

Discrete anisotropic radiative transfer (DART) calibration [28]–[30] can open new avenues to improve the retrieval of urban SS, which allows the variation of endmember from pixel to pixel when retrieving SS of urban components. This 3-D radiative transfer model was selected because it offers the advantage of working with any satellite image characteristics (spatial resolution, spectral band, etc.) and any urban architecture [31]–[34]. Indeed, it can simulate remote sensing images considering multiple scattering events between the urban components [35], [36]. It has been widely used for remote sensing studies, including vegetation [37], [38] and cities [39]. In addition, the DART calibration has already been successfully used in urban studies to map urban albedo and 3-D shortwave radiative budgets [30].

However, a current validation of DART calibration is still lacking. Up to now, its only validation was done by comparing the time series of the radiative budget Q^*_{SW} simulated by DART and measured by flux towers in Basel, Switzerland. Therefore, a more comprehensive accuracy analysis is essential for DART calibration. This article focuses on quantitative analysis of DART calibration accuracy under various situations. It also investigates the factors that impact DART calibration accuracy. This article is a synthetic study because DART simulated images mimic satellite images. First, in the so-called "ideal case," the SS of the urban components are the only unknowns. Then, in a "nonideal case," we consider that a number of parameters associated with satellite observations are not perfectly known. Finally, we give an example of employing DART calibration in one PlanetScope image to retrieve SS of land covers.

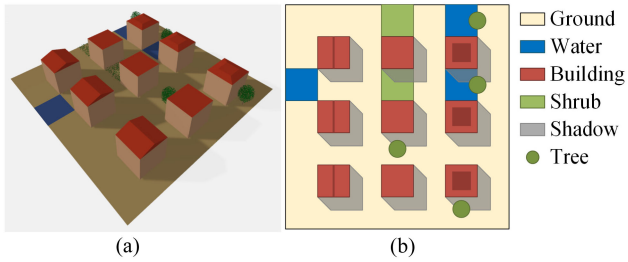

Fig. 1. Schematic urban scene: ground, water, shrubs, trees, and buildings with flat, triangular prism, and frustum of a square pyramid roofs. (a) 3-D view. (b) Top view.

II. Materials and Methods

A. Description of the Urban Scene

The study site was a synthetic 128 m × 128 m 3-D urban scene with five types of components: flat ground; water; buildings; shrubs; and trees (see Fig. 1). There were three 15 m × 15 m water surface (opaque) and nine buildings with three kinds of roofs evenly distributed in the scene. Roofs were triangular prism on the left side of the scene, flat in the middle, and frustum of a square pyramid on the right with the same inclination equal to 20°. The length, width, and height of the buildings were 15 m, and the length and width of the ground surfaces between the buildings were also 15 m. These are common values in European cities [40].

The scene contained two shrubs whose length and width were 15 m with a 1 m height. The shrub was modeled as a uniform volume of leaf elements with a spherical leaf angle distribution (LAD) and a leaf area density equal to 0.5 m^2/m^3. The scene also contained four trees. In order to simplify the analysis of the inversion procedure, these trees were directly created by DART and not imported. In addition, the foliar elements of the tree crowns and shrubs were simulated with small triangles and not with a turbid medium. The trees created with DART have trunks simulated with frustum of a octagon pyramid and crowns with specific vertical and horizontal profiles of LAD and the volume density of the leaf area. Here, all trees had the same geometric parameters: an ellipsoidal crown with 10 m height and 10 m diameter at mid-height and homogeneously filled with a 0.5 m^2/m^3 leaf density. The urban components were spatially distributed to meet the usual illumination conditions with shadows and mixed pixels effects.

B. DART Calibration

DART calibration is an iterative inversion method applied to a satellite image to get a map of SS per type of urban component with urban anthropogenic heat flux. DART calibration first retrieves the SS of endmembers by iteratively comparing simulated and satellite images. Then, this 2-D component SS map allows one to compute anthropogenic heat flux maps. The retrieved procedure comprises two major steps.

The first step provides first order SS maps using the LSMA method. DART estimates the "amount" of urban components by simulating a reflectance image and an image per type of urban component called "component reflectance image." The term "amount" indicates the spectral contribution of each component

TABLE I
INPUT SS PARAMETERS FOR THE DART CALIBRATION PROCEDURE. ρ MEANS REFLECTANCE AND τ MEANS TRANSMISSIVITY. SWIR MEANS SHORT WAVE INFRARED

Components SS		Ground	Roof	Shrub	Water	Tree (ρ+τ)
Initial SS for base simulation	Blue (492.4±66 nm)	0.2169	0.0748	0.1173	0.0695	0.3578
	Green (559.8±36 nm)	0.2483	0.1122	0.2635	0.0649	0.4600
	Red (664.6±31 nm)	0.2561	0.2501	0.0987	0.0543	0.6140
	NIR (832.8±106 nm)	0.2366	0.3100	0.9289	0.0283	0.9289
	SWIR1 (1613.7±91 nm)	0.2011	0.7165	0.6794	0.0053	0.8722
	SWIR2 (2202.4±175 nm)	0.1693	0.7190	0.4178	0.0051	0.6497
Pseudo image SS for satellite simulation	Blue (492.4±66 nm)	0.0574	0.1067 0.1131 0.0574	0.0927 0.0536	0.0277 0.0364 0.0326	0.1153 0.0829
	Green (559.8±36 nm)	0.0710	0.1456 0.1206 0.0710	0.1996 0.1329	0.0269 0.0250 0.0380	0.1733 0.1942
	Red (664.6±31 nm)	0.1003	0.3074 0.1308 0.1003	0.0892 0.0405	0.0267 0.0206 0.0245	0.0854 0.0820
	NIR (832.8±106 nm)	0.1681	0.3257 0.1460 0.1681	0.9426 0.9013	0.0262 0.0198 0.0198	0.9596 0.9013
	SWIR1 (1613.7±91 nm)	0.3349	0.3623 0.1049 0.3349	0.5631 0.5551	0.0210 0.0186 0.0186	0.5199 0.6668
	SWIR2 (2202.4±175 nm)	0.2635	0.3213 0.1009 0.2635	0.3091 0.2494	0.0189 0.0163 0.0163	0.2778 0.4911

and not its relative area proportion. Therefore, its meaning differs from the term "abundance," and the presence of multiple scattering explains that the sum of the "amount" of all components can be larger than one. The inversion method starts with user-defined SS values that can be selected from the DART database. First-order SS maps are calculated by assuming that all urban components of the same type share the same SS within a certain distance. In this step, the urban components with a small amount are neglected for each pixel because they are difficult to assess. Here, we used a threshold of 1%.

The second step is a sequence of iterations that converge towards a final SS map per type of urban component at the satellite image spatial resolution. It combines the bisection and Newton's methods. The SS is the independent variable, and the component reflectance image is a dependent variable. Basically, if the reflectance of a DART pixel is smaller than that of the satellite image, the SS values of the components in this pixel are increased, and vice versa. It is operated per pixel. The SS values of the components in a pixel are no longer updated in the following iterations if the relative difference of the DART and satellite pixel reflectance is less than a user-defined threshold; here, this threshold was set to 1%. This step implicitly considers multiple scattering between components. At the end of the procedure, the DART image simulated with the retrieved SS maps is nearly equal to the satellite image (i.e., mean relative error smaller than 10^{-3}). A detailed description of DART calibration is in the literature [28]–[30].

The accuracy of the DART calibration method was assessed using a DART simulated image that mimics an atmospherically corrected satellite image. Therefore, DART computed two products: the pseudo satellite image and the so-called base image that converges to the pseudo satellite image with the iterative change of the component SS maps by the calibration method. The relative difference between the true and retrieved SS values was used to indicate the DART calibration accuracy. Six spectral bands (three visible bands, near-infrared band (NIR), and two short wave infrared bands) were considered. It must be noted that DART calibration processes all bands independently; it can process monoband images. Also, the DART atmosphere radiative transfer module [41], [42] was not used because the satellite image was assumed to be atmospherically corrected.

As already mentioned, two cases of base simulations were studied: an ideal case and a nonideal case. In the ideal case, SS values were the only unknowns (see Table I). All other input parameters were identical between the base and satellite simulations: 30° solar zenith angle (SZA); perfect sensor modulation transfer function (MTF), 4 m satellite image spatial resolution, perfect geometric registration of the base and satellite images, etc., (see Table II). SZA greatly influences the bidirectional reflectance effect [43]–[45] by distributing shadows in the image. Besides, together with the roof inclination, they determine the angle of incidence of light hitting the roof. The MTF defines how much contrast the sensor retains to the original target. It defines the faithful transition of the object's spatial frequency content of the image. It can blur the image and thus affect SS retrieval accuracy [46]. Spatial resolution refers to the dimension of a pixel on the ground.

The nonideal case considered the complexity of the satellite image. Indeed, several satellite observation factors, used as DART input parameters of the base image, could not be precisely known. Their imprecision influenced the retrieval of SS. The six considered influence factors corresponded to two broad

TABLE II
INPUT SIMULATION PARAMETERS FOR THE DART CALIBRATION PROCEDURE

Parameters	Ideal-case	Non-ideal-case	
MTF	1	0.15 - 0.3	
SZA	30°	0 - 60°	
Spatial resolution	4 m	0.5 - 15 m	The step of each input parameter is determined by eFAST sensitivity analysis.
X-axis shift	0 pixel	0 - 1 pixel	
Y-axis shift	0 pixel	0 - 1 pixel	
Urban geometry accuracy	100%	95% - 105%	

categories: Image acquisition: SZA; image spatial resolution; and MTF. Accuracy in image registration (x- and y-shift) and 3-D geometry of the urban scene.

In the nonideal case, SZA and spatial resolution of the satellite image were identical in the pseudo and base images because they were usually known. Conversely, MTF, registration errors, and the accuracy of 3-D objects were often not well known. Therefore, they differed between satellite and base simulations. MTF was simulated using the Gaussian filter but was only used in the satellite simulation because the current DART calibration method did not consider it in the inversion process. Similarly, the geometric registration of satellite images and the geometry of 3-D urban scenes could not be perfectly known. Therefore, they were fixed in the satellite simulation while varying in the base simulation to mimic geometry inaccuracy. A total of 70 samples were generated per influence factor (see Table II), which led to 420 samples. The range of MTF was set to 0.15–0.3, corresponding to the 10 m spatial resolution band of Sentinel-2 images [47]. The range of SZA was set to 0°–60°. The range of spatial resolution was set to 0.5–15 m, corresponding to most high-resolution satellites, including Satellite Pour l'Observation de la Terre (SPOT), RapidEye, Advanced Land Observing Satellite (Alos), Ziyuan-3 (ZY3), Gaofen-1 (GF1), Keyhole (KH), IKONOS, QuickBird, WorldView, GeoEye, and Pleiades. According to the literature [48], [49], the geo-positioning accuracy of satellite images can be subpixel. Therefore, the maximal range of pixel-shift was set to one pixel. Besides, the input parameters (e.g., geometry of buildings, trees, water surfaces, and tree leaf area) used to construct the 3-D landscape could not be precisely known. Therefore, in the base simulations of the nonideal case, these parameters were varied with factors from 95% to 105% compared to the pseudo satellite simulation.

C. Sensitivity Analysis

Model sensitivity analysis focused on the effect of differences in the values of DART input parameters on the retrieved SS accuracy. A global sensitivity analysis was done for the non-ideal-case only. A global sensitivity analysis model, called the extended Fourier amplitude sensitivity test (eFAST) [50], was used to assess the influence of each factor mentioned above: MTF, SZA, satellite spatial resolution, registration error x and y, and imprecision of 3-D objects.

The eFAST is a sensitivity analysis method based on numerical computations for the predicted value and variance of a model prediction. The basis of the calculation is to turn a multidimensional problem into a 1-D integral over all unknown model inputs. To avoid multidimensional integration, a search curve that passes through the entire parameter space is created. The decomposition of the Fourier series representation is used to obtain the fractional contribution of individual input variables to model prediction variance. The analysis consisted of four stages.

1) Building the ranges and distributions for the input parameters and formally developing the predicted value and output variance in terms of integrals for the input parameter space.

2) Transforming the given multidimensional integral into a single-dimensional integral on input parameter space.

3) Estimating the predicted value and performance variance.

4) Estimating the sensitivity indices.

First-order sensitivity indices and total indices are computed using the Fourier decomposition terms of the model output [51]. First-order sensitivity indices are a direct measure of sensitivity based on variance and contribute to the output variance of the principal effect of an input parameter. As a result, it measures the effect of variation of an input parameter only but averaged over the variations of other input parameters. Total order sensitivity indices measure each input parameter's contribution to the output variation, including all variances produced by its interactions with other input variables in any order.

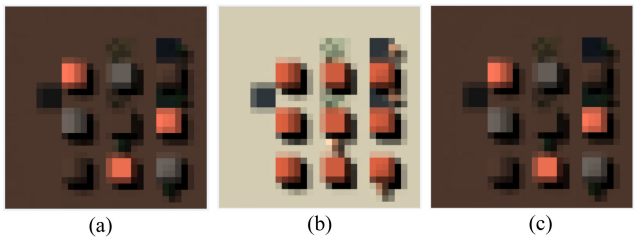

Fig. 2. (a) DART pseudo satellite image of the 3-D scene. It has some spectral confusions (e.g., the different reflectance for nine roofs and the same reflectance of three roofs as ground reflectance). (b) DART image simulated with constant SS per urban component. (c) DART image after the calibration procedure. All images are RGB color composites.

III. RESULTS

A. Accuracy Assessment: Ideal Case

Fig. 2 shows the pseudo satellite image and the associated base images before and after calibration. In the pseudo satellite image, the roofs had reflectance values that differed and could be close to those of the ground conversely to the uncalibrated base image, where all roofs had the same reflectance. As expected, the calibrated base image was visually very similar to the pseudo satellite image. Fig. 3 shows the evolution of the mean absolute value of the relative error $\overline{|\varepsilon|}_{\text{component}}$ per component with iterations of the calibration method in the green band. For each component, $\overline{|\varepsilon|}_{\text{component}}$ was very large in the uncalibrated image (ground: 13.08, roof: 8.72, water: 33.88, tree: 4.47, shrub: 5.27). It dramatically decreased down to around 0.01

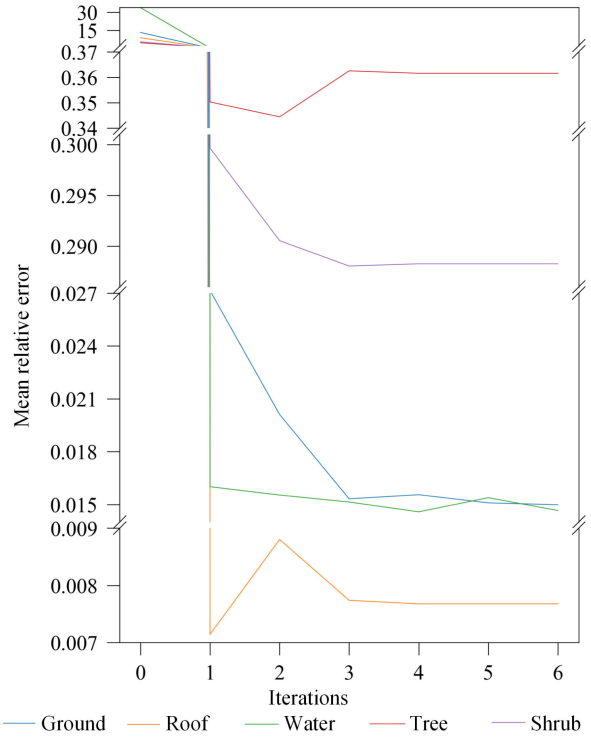

Fig. 3. Evolutions of the mean absolute value of the relative error of the component SS with the iterations in the green band. The mean absolute value of the relative error at iteration 0 is due to the selected initial SS value. Relative errors are calculated pixelwise for each component, and a mean statistical value of the absolute value of the relative error is calculated. Similar trends are found in the other bands.

for ground, roof, and water in the calibrated image. However, it only decreased down to 0.29 for shrubs and 0.36 for trees. Besides, for the trees, this decreased oscillates with iterations.

Fig. 4 shows spatial images and violin diagrams of the relative error of each component in the calibrated image. The calibration appeared to be more accurate for pure pixels than for mixed pixels: $\overline{|\varepsilon|}_{\text{pure ground}} = 0.0065$ with $\overline{|\varepsilon|}_{\text{mixed ground}} = 0.0693$, $\overline{|\varepsilon|}_{\text{pure roof}} = 0.0070$ with $\overline{|\varepsilon|}_{\text{mixed roof}} = 0.0089$, $\overline{|\varepsilon|}_{\text{pure water}} = 0.0015$ with $\overline{|\varepsilon|}_{\text{mixed water}} = 0.0268$, and $\overline{|\varepsilon|}_{\text{pure tree}} = 0.2519$ with $\overline{|\varepsilon|}_{\text{mixed tree}} = 0.3806$. Besides, the accuracy of SS is very similar in the sunlit and shaded areas. In addition, an initial SS confusion had a negligible impact on $\varepsilon_{\text{component}}$. Results for ground [see Fig. 4(a) and (b)] were excellent, even for shaded ground, except for mixed pixels with vegetation. Results were also good for roofs [see Fig. 4(c) and (d)] and water surfaces [see Fig. 4(e) and (f)], even in shaded areas, except for mixed water pixels containing vegetation. The shape of roofs had a negligible impact on $\varepsilon_{\text{roof}}$. However, the performances of vegetation include shrub [see Fig. 4(g) and (h)] and trees [see Fig. 4(i) and (j)], were relatively unideal compared to others.

B. Sensitivity Analysis and Accuracy Assessment: Nonideal Case

1) Sensitivity Analysis: A sensitivity study was performed on the nonideal case. Fig. 3 indicates that the calibration procedure nearly converges at iteration five. Therefore, we set a constant maximum iteration value of eight for all sensitivity analyses.

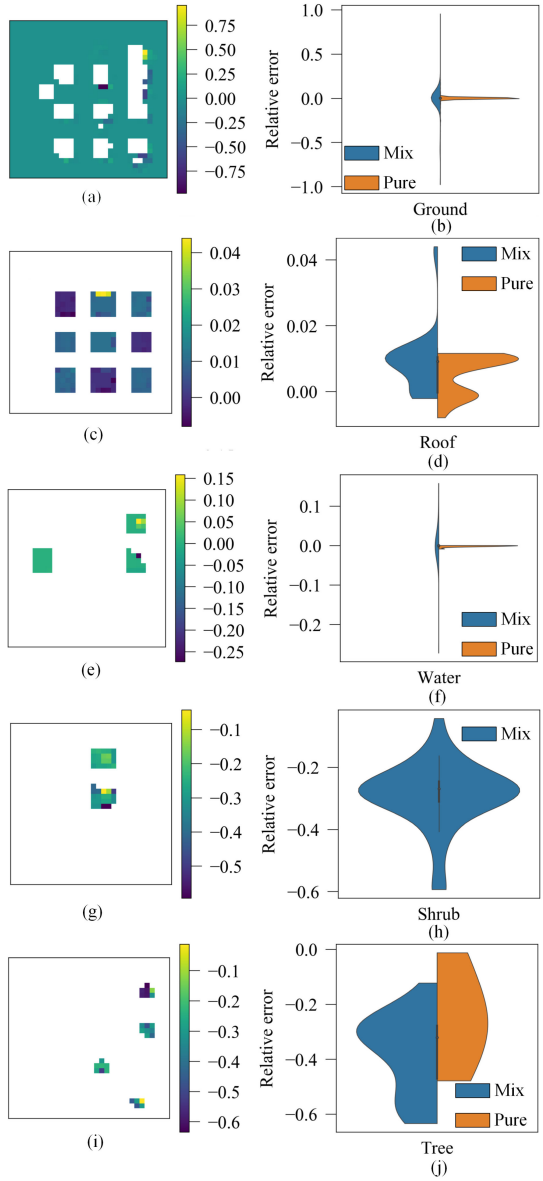

Fig. 4. Final calibration results of the error analysis for ground (a and b), roof (c and d), water (e and f), shrub (g and h), and trees (i and j) in the green band in the spatial and frequency domain. Relative errors are calculated pixelwise. Blank in the image means there is no corresponding component in that pixel. Violin range is limited to within the range of the relative error. A similar phenomenon was also observed for other bands.

SZA, satellite image resolution, pixel-shift, landscape modeling inaccuracy, and MTF were analyzed using eFAST sensitivity analyses (see Fig. 5).

Modulation Transfer Function: The result shows that MTF had very little influence on the calibration accuracy. The highest mean first-order sensitivity (0.095) and total order sensitivity (0.658) over all bands was the shrub. The lowest mean first order sensitivity (0.018) and total order sensitivity (0.093) over all bands was ground. The MTF mean first order and total order sensitivity over all bands over all components were 0.056 and 0.346.

Solar Zenith Angle: Ground had the highest mean first order sensitivity (0.721) and the mean total order sensitivity (0.861)

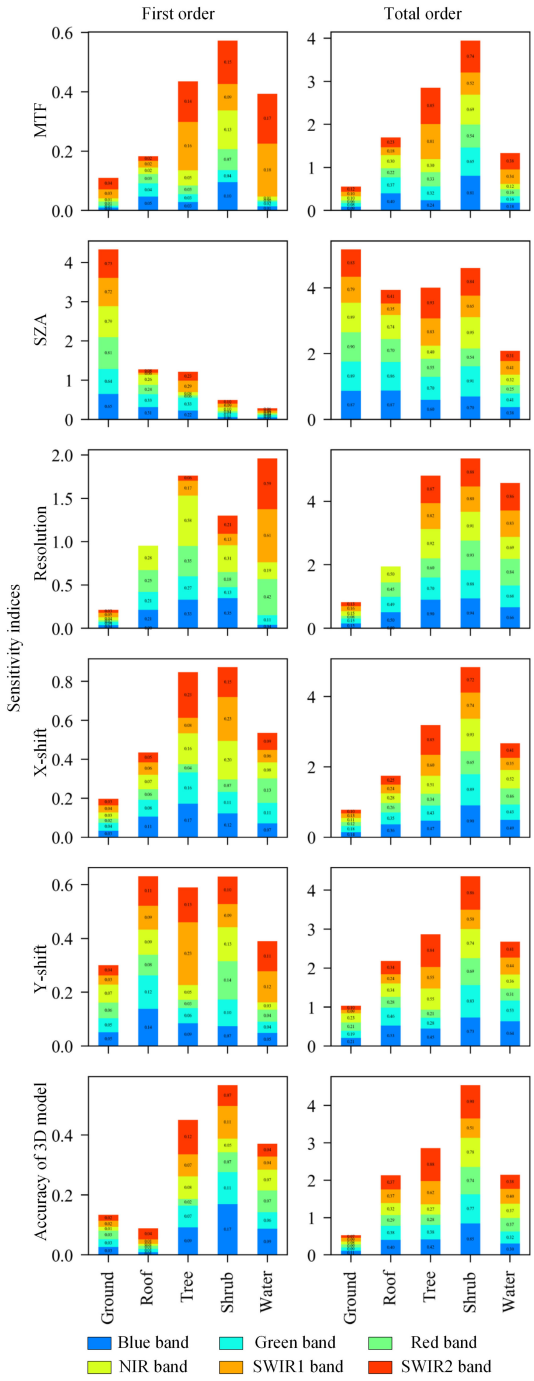

Fig. 5. Sensitivity analysis results. The eFAST method is used for sensitivity analysis based on 420 cases. Sensitivity indices are calculated per component per band and stacked over all bands. All subplots share the same *x*-axis. The effect magnitudes are SZA, satellite spatial resolution, pixel-shift, landscape model inaccuracy, and MTF, in descending order of magnitude.

over all bands. Water had the lowest mean first order sensitivity (0.047) and the mean total order sensitivity (0.348) over all bands. Overall, the SZA mean first order and total order sensitivity over all bands were 0.253 and 0.660, respectively.

Satellite Resolution: Water had the highest mean first order sensitivity (0.327) over all bands, and shrub had the highest mean total order sensitivity (0.891) over all bands. The lowest mean first order sensitivity (0.036) and total order sensitivity (0.137) over all bands was ground. The mean first order and total order sensitivity of the spatial resolution over all bands were 0.222 and 0.628.

X-shift: The highest mean first order sensitivity (0.145) and total order sensitivity (0.806) over all bands was the shrub. The lowest mean first order sensitivity (0.033) and total order sensitivity (0.129) over all bands was ground. The X-shift mean first order and total order sensitivity over all bands over all components were 0.096 and 0.441, respectively.

Y-shift: The roof had the highest mean first order sensitivity (0.105) over all bands, and the shrub had the highest mean total order sensitivity (0.727) over all bands. The lowest mean first order sensitivity (0.050) and total order sensitivity (0.172) over all bands was ground. The Y-shift mean first order and total order sensitivity over all bands over all components were 0.085 and 0.437.

Accuracy of the 3-D scene model: The highest mean first order sensitivity (0.094) and total order sensitivity (0.758) over all bands was the shrub. The roof had the lowest mean first order sensitivity (0.015) over all bands, and the ground had the lowest mean total order sensitivity (0.088) over all bands. The accuracy of the 3-D scene model mean first order and total order sensitivity over all bands over all components were 0.054 and 0.407.

Overall, mean sensitivity values over all components were close to each other for the six bands: 0.317 for the blue band; 0.305 for the green band; 0.307 for the red band; 0.264 for the NIR; 0.301 for the short wave infrared 1 (SWIR1) band; and 0.342 for the short wave infrared 2 (SWIR2) band. Besides, the mean total order sensitivity (0.485) was four times larger than the mean first order sensitivity (0.127) over all bands and over all components.

2) Accuracy assessment: Nonideal Case: Fig. 6 shows the mean absolute value of the relative error per component over all 420 cases. Performances were excellent in all bands for ground and roof: the range of $\overline{|\varepsilon|}$ was 0.015–1.572 for ground and 0.024–1.7662 for roofs. The accuracies were less accurate for the other components than ground and roof, especially for components in the band with low SS. Large errors tended to occur if the SS of the component was low. For example, for vegetation (i.e., shrubs, trees), the range of $\overline{|\varepsilon|}$ was 0.159–2.709 in the green band. However, its range in the red band was even 0.341–11.445. Similarly, $\overline{|\varepsilon|}_{\text{water}}$ increased dramatically in SWIR1 and SWIR2, where its SS is low. The range of $\overline{|\varepsilon|}_{\text{water}}$ over all bands was 0.053–15.683.

IV. Satellite Image Application

The DART calibration was also applied to real satellite data to verify its accuracy preliminarily. The study area was selected as Basel, a research target of the URBan ANthropogenic heat FLUX from the Earth observation Satellites (URBANFLUXES) project [52]. Basel is a city in northwestern Switzerland on the river Rhine, where the Swiss, French, and German borders meet [28], [30]. Our study area comprised almost the entire city of Basel, with latitude from 47.53°N to 47.57°N, and longitude from 7.55°E to 7.62°E. Its geometric database was very detailed (see Fig. 7). These cities are characteristic European cities to allow the extension of the results to other European cities. Their

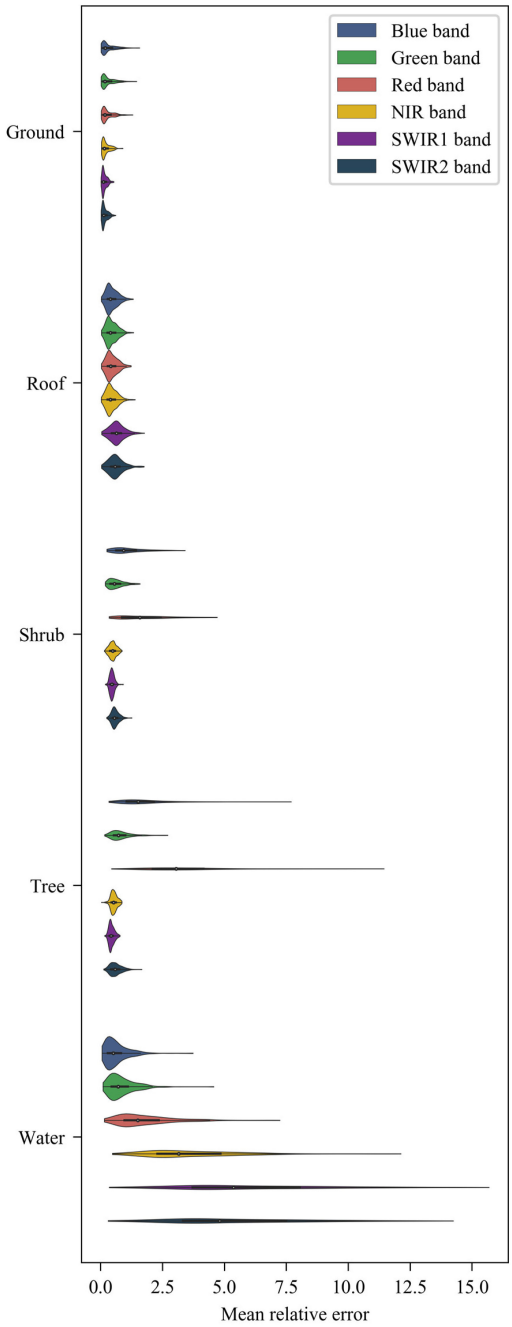

Fig. 6. Mean absolute value of the relative errors on the retrieved SS of scene components for the blue, green, red, NIR, SWIR1, and SWIR2 bands. Relative errors are calculated pixelwise per component. The absolute value of relative error is averaged over all 420 cases. Violin range is limited to within the range of the mean absolute value of the relative error.

3-D mock-ups were initially constructed and used by Landier *et al.* [28]–[30]. The land cover classes of Basel included buildings, impervious layer, water, low vegetations, bare soils, deciduous, and evergreen, according to the URBANFLUXES project [53], [54]. Here, some classes were grouped. The tree class contained deciduous and evergreen; the ground class contained impervious surface, low vegetations, and bare soils; and the building and water classes were the same as in the URBANFLUXES project. The location and geometric structure

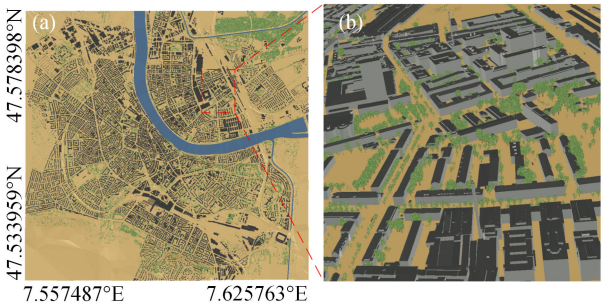

Fig. 7. Basel 3-D scene. (a) Top view. (b) Side view of the red square in (a). Buildings (roofs: dark, walls: light grey), trees (green), river (blue), and ground (yellow).

TABLE III
SATELLITE IMAGE PARAMETERS

Parameters	Values			
ID	20190915_100328_1003			
Date	Sep 15, 2019, 10:03:28 UTC			
Source	4-band PlanetScope Scene			
Cloud percentage	0%			
Pixel resolution	3 m			
Satellite ID	1003			
Off-nadir angle	0.0°			
Sun elevation	42.2°			
Sun azimuth	152.0°			
Instrument	PS2			
Spectral bands (nm)	Blue	Green	Red	NIR
	455 - 515	500 - 590	590 - 670	780 - 860

of all urban components, including the local digital elevation model (DEM), were from the local city database. Trees were defined by their location, height, and crown dimensions from field measurements. DART simulated trunks with frustum of a octagon pyramid and crowns as ellipsoidal volumes filled with small triangles in this work. Here we only give necessary information about the city database. More detailed descriptions are presented in the literature [28].

We downloaded one 3 m resolution multispectral surface reflectance image with four bands from Planet (https://www.planet.com/). This image had undergone orthocorrection and atmospheric correction, and it was selected because its off-nadir angle was precisely 0.0. Table III gives the detailed parameters of this image. Data processing included geometry co-registration between satellite images and DART simulated images. We first clipped the satellite images based on the geographical latitude and longitude and kept only the remote sensing images in the study area. Then we shifted the 3-D urban database along the x- and y-axis to do the co-registration between the DART image and the satellite image. Satellite images were distorted due to factors such as observation angle and image distortion. Therefore, the geometric accuracy of DART simulated images was much higher than that of satellite images. We set the DART simulated image as the base image and used the GeFolki [48], [49] developed by the French aerospace lab to warp the satellite image to DART simulated image for co-registration. Gefolki is a module allowing carrying out the co-registration of two remote sensing images with a geometry accuracy of less than 0.1 pixels. Finally, the warped satellite image was used for inversion with DART simulated image.

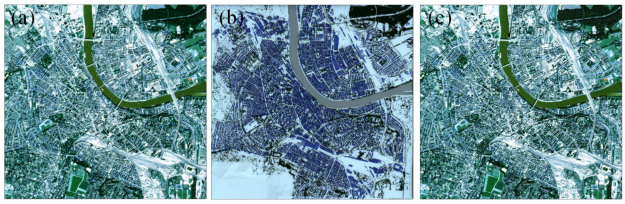

Fig. 8. (a) PlanetScope image in the Basel area. (b) DART image simulated with constant SS per urban component. (c) DART image after the calibration procedure. All images are RGB color composites.

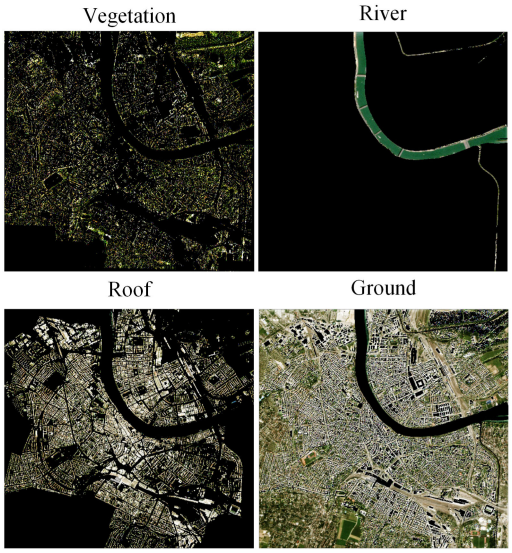

Fig. 9. Retrieved SS of vegetation, river, roof, and ground by DART calibration. All images are RGB color composites. The black pixels indicate no corresponding element in that pixel.

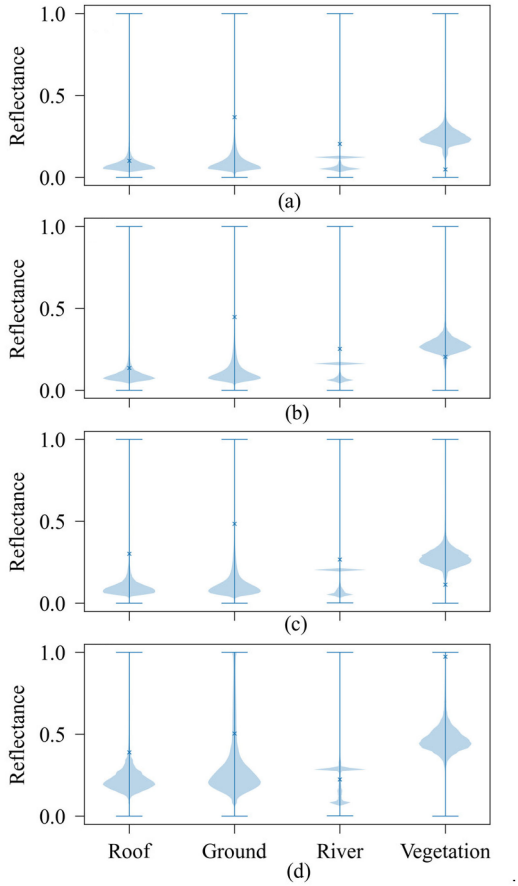

Fig. 10. Frequency distribution of SS obtained from DART calibration in (a) blue, (b) green, (c) red, and (d) NIR bands. The cross symbol indicates the SS in iteration 0 of DART calibration in Fig. 8(b).

Subarctic summer was selected as the atmosphere model in the DART simulation. This atmospheric model was selected using the total column water vapor and air temperature [55]. These data were from water vapor and surface temperature data of the National Centers for Environmental Prediction and the National Center for Atmospheric Research reanalysis data [56]. The aerosol model was selected as urban mode based on the study area directly [55]. As atmospherically corrected surface reflectance data were used, we assumed that the atmospheric influence was removed, so the atmospheric parameters have minimal effect on the results (only the skylight distribution is affected). The input parameters of spectral bands, spatial resolution, and sun-target-satellite geometry were kept consistent with the satellite image in the DART simulation (see Table III).

Fig. 8 shows the satellite image and DART simulated images before and after DART calibration. Before calibration, the difference between DART simulated image and the satellite image was tremendous. However, after calibration, the difference was tiny. Figs. 9 and 10 depict the SS distribution in spatial and frequency. We carefully examined the bimodal issue for the water bodies and found that it was due to the lack of bridges in the urban 3-D structure database, and therefore some of the reflectance values of the bridges were assigned to the water body. Also, some ground pixels showed typical vegetation SSs (some pixels were very green in Fig. 9). It is because, in our city 3-D database, there was no distinction between ground and grassland. Therefore, during the DART radiative transfer simulation, the grassland pixels were also considered as a opaque surface. In all, there were significant spectral differences between the different components, indicating good spectral unmixing.

V. Discussion and Conclusion

A. Discussion

1) Accuracy Assessment: The DART calibration method has only been validated by comparing the time series of the short wave radiative budget Q^*_{SW} simulated by DART and measured in a flux tower in Basel, Switzerland [30]. The mean relative difference over one year was 2.7%, which is a very encouraging result. However, this comparison was only a kind of one-pixel validation. Here, the validation is extended to every pixel by using a DART simulated pseudo satellite image.

Our results [see Figs. 2 and 3] show that the DART calibration has an excellent overall accuracy under ideal experimental conditions. However, vegetation has a markedly less accurate retrieved SS compared to other urban components. Three explanations are put forward.

1) Being a volume of foliar elements, vegetation cannot be simulated as a simple surface like the other urban components.

2) The leaf SS includes leaf transmittance and reflectance. Here, it is represented by the leaf single scattering albedo, with a predefined spectral ratio between its reflectance and transmittance.

3) The low value of leaf SS in the considered spectral bands.

Other works already stressed the poor performance of vegetation in the unmixing model [21], especially for mixed pixels that contain vegetation. The complexity of vegetation structure, including multiple scattering, leads to complex nonlinear relationships between leaf albedo and canopy reflectance [57], [58]. These remarks are consistent because the DART calibration provides maps of SS that are less accurate for vegetation than for urban surface components such as ground and roofs. Similarly, the low reflectance of water complexifies the retrieval of its SS [21]. However, here, the results are excellent for water, even in shaded areas (see Fig. 4). It is explained that water surfaces are treated as opaque surfaces in this article.

Shadows are usually mentioned as an essential source of inaccuracy in the retrieved SS [59]. For example, shadows cast by buildings in urban densities considerably obscure local information in the image, leading to possibly corrupted results or interpretative errors [60]. Methods like MESMA try to solve this problem by incorporating shade as an endmember [21]. Here, the impact of shadows on the retrieval of SS is relatively low, suggesting that the algorithm of DART calibration is well adapted to the processing of shaded urban areas.

The nonideal case stresses that inaccurate DART input parameters can significantly affect the calibration accuracy (see Fig. 6). For example, an inaccurate geometric co-registration of the satellite image leads to an inaccurate amount estimation and finally leads to the poor estimation of SS. In contrast to some traditional hybrid image unmixing, DART calibration does not estimate the abundance calculated from the endmember SS, which is a significant advantage because it allows the SS of the endmember to vary from pixel to pixel. However, it needs a very accurate co-registration of the satellite image and the 3-D scene model. Besides, we find that some components with low SS (e.g., water and vegetation) produce high relative error and variance. It is because we use the relative error, and if the pixel shifting problem leads a high reflectance pixel to a low SS component, the denominator is too small in relative error, leading to the high relative error and variance.

2) Sensitivity Analysis: DART calibration accuracy is influenced by SZA, satellite spatial resolution, pixel shift, landscape model inaccuracy, and MTF in descending order of magnitude (see Fig. 5). SZA significantly impacted ground apparent reflectance through shadows and bidirectional reflectance effects. Also, for the roofs, SZA and the angle of the inclined roofs determine the incidence angle. The low sensitivity of SZA on water may be that water was treated as opaque surfaces without topography in our article.

The spatial resolution of satellite imagery is an essential factor in city studies because it determines the pure pixel distribution in the satellite image [21]. High-resolution sensors tended to produce pure pixels, while low-resolution sensors were more likely to produce mixed pixels. Welch [61] uses average urban plots to demonstrate that the high-frequency details that characterize the urban scene are necessary for remote sensor data with spatial resolutions of 0.5–10 m. A spatial resolution of at least 5 m is needed to capture urban structures for urban applications adequately [62]. The spatial resolution of the image is also a constraint on DART calibration because it assumes that the SS of components in a pixel is constant in this pixel. A potential solution could be to subclassify urban components. For example, roofs in the same pixel could be classified into subcomponents if additional information (e.g., type of material) is available. Moreover, this assumption can also be mitigated with higher image resolution.

Pixel shifting has little impact on the inversion accuracy of continuous and homogeneous components (e.g., ground), and it is the same for the accuracy of the 3-D model because they had similar geometric effects on the amount estimation problem of mixed pixels. MTF had less impact on large and homogeneous scene components such as ground than on small components such as roofs, trees, water, and shrubs. In all, the components with small size and high heterogeneity are much more sensitive than components with big size and high homogeneity.

3) Satellite Image Application: It should be noted that in our work, we use a satellite image with off-nadir angle equal to 0.0°. The primary difficulty in using the off-nadir image is the inconsistent coordinate system between satellite image and DART simulated image. Most surface reflectance satellite products (e.g., Sentinel 2 L1C product with the date before March 2021, https://sentinel.esa.int/web/sentinel/user-guides/sentinel-2-msi/definitions) using DEM to do orthorectification, and this rectification is called "orthorectification." As a result, some buildings are tilted in the image (the walls can be seen in the image). However, the DART module uses digital surface model (DSM) to do orthorectification, and this rectification is called "true orthorectification." As a result, all the buildings are vertical (There are no wall pixels in the simulated image). The coordinates of the corresponding image points in the two kinds of images are different. However, geometry accuracy is critical for DART calibration, especially for the scene with strong heterogeneity. Research is being conducted for the DART model to provide an "orthorectification" image in addition to the "true orthorectification" image.

B. Conclusion

We assessed the accuracy of the DART calibration to retrieve SS per component of an urban scene, for an ideal case (i.e., SS is only unknown) and a nonideal case (i.e., SS is unknown with inaccurate input parameters), for the visible, NIR and two SWIR band. Sensitivity analyzes were also done on some parameters. The major conclusions are as follows.

1) Calibration accuracy is influenced by SZA, satellite spatial resolution, pixel shift, landscape model inaccuracy, and MTF in descending order of magnitude.
2) In the ideal case, the mean absolute value of the relative error over all bands of ground, roof, water, tree, and shrub is 0.013, 0.005, 0.027, 0.297, and 0.250, respectively. It is 0.233, 0.507, 3.088, 0.834, and 1.256 in the nonideal case.
3) Calibration is insensitive to the number of bands and is highly resistant to shadow interference.
4) Some uncontrollable external factors may be significant to the accuracy image, such as co-registration error or the user-defined ratio between leaf reflectance and transmittance.

Overall, the DART calibration (i.e., retrieval of SS maps of urban components from remote sensing images) is generic, accurate in ideal cases, and efficient in handling interclass spectral confusion. Besides, present improvements in co-registration procedures increase its potential. Its applications are numerous. Indeed, the availability of up-to-date SS maps of urban scenes using a time series of satellite imagery is valuable in many domains, such as urban management and urban climate. For example, it is essential for computing the urban radiative budget, and consequently, the urban energy budget and associated heat fluxes. Therefore, it helps to address significant issues facing cities, such as urban climate and change detection.

Compared with the traditional spectral unmixing models that can only identify the variability of endmember spectra only within the interclass, DART calibration can identify the variability of endmember spectra between pixels, which is extremely helpful for studying high heterogeneous urban areas. Another advantage of the DART calibration should be noted: it does not need hyperspectral images because it can work with a single band image. Therefore, it is well adapted to satellites with few spectral bands with a high spatial resolution (e.g., Sentinel-2).

To upscale from micro to local scale, spectral un-mixing approaches and radiative transfer modeling have been used in past studies, with DART model to be the most comprehensive physical modeling scheme [52]. A limitation in this article is that DART calibration directly upscales to pixel level through material fractions via spectral mixture analysis. The radiative transfer of facet is implicitly considered in the simulation to calculate "amount" because DART computations (e.g., scattering and absorption) are done at the facet level. Another interesting idea to retrieve SS of components might be making all calculations at the facet level first and then upscale to the pixel level. In this case, the urban morphology effect could be implicitly included in the up-scaling procedure.

ACKNOWLEDGMENT

The authors would like to thank Dr. L. Landier in CNES for his initial work on DART calibration, to the reviewers and the editor for valuable comments and suggestions to improve the manuscript.

REFERENCES

[1] J. Li, P. Gamba, and A. Plaza, "A novel semi-supervised method for obtaining finer resolution urban extents exploiting coarser resolution maps," *IEEE J. Sel. Topics Appl. Earth Observ.*, vol. 7, no. 10, pp. 4276–4287, Oct. 2014.

[2] J.-P. Gastellu-Etchegorry, "3D modeling of satellite spectral images, radiation budget and energy budget of urban landscapes," *Meteorol. Atmos. Phys.,* vol. 102, no. 3/4, pp. 187–207, 2008.

[3] M. Herold, D. A. Roberts, M. E. Gardner, and P. E. Dennison, "Spectrometry for urban area remote sensing—Development and analysis of a spectral library from 350 to 2400 nm," *Remote Sens. Environ.,* vol. 91, no. 3/4, pp. 304–319, 2004.

[4] S. Kotthaus, T. E. Smith, M. J. Wooster, and C. Grimmond, "Derivation of an urban materials spectral library through emittance and reflectance spectroscopy," *ISPRS J. Photogramm. Remote Sens.,* vol. 94, pp. 194–212, 2014.

[5] J. Li, M. Khodadadzadeh, A. Plaza, X. Jia, and J. M. Bioucas-Dias, "A discontinuity preserving relaxation scheme for spectral–spatial hyperspectral image classification," *IEEE J. Sel. Topics Appl. Earth Observ.*, vol. 9, no. 2, pp. 625–639, Feb. 2016.

[6] M. O. Mughal *et al.*, "High-resolution, multilayer modeling of singapore's urban climate incorporating local climate zones," *J. Geophys. Res., Atmos.,* vol. 124, no. 14, pp. 7764–7785, 2019.

[7] B. Cao *et al.*, "A review of earth surface thermal radiation directionality observing and modeling: Historical development, current status and perspectives," *Remote Sens. Environ.,* vol. 232, 2019, Art. no. 111304.

[8] J.-P. Gastellu-Etchegorry *et al.*, "Discrete anisotropic radiative transfer (DART 5) for modeling airborne and satellite spectroradiometer and LIDAR acquisitions of natural and urban landscapes," *Remote Sens.,* vol. 7, no. 2, pp. 1667–1701, 2015.

[9] Q. Weng and D. Lu, "Landscape as a continuum: An examination of the urban landscape structures and dynamics of indianapolis city, 1991–2000, by using satellite images," *Int. J. Remote Sens.,* vol. 30, no. 10, pp. 2547–2577, 2009.

[10] J. Li, J. M. Bioucas-Dias, A. Plaza, and L. Liu, "Robust collaborative nonnegative matrix factorization for hyperspectral unmixing," *IEEE Trans. Geosci. Remote Sens.,* vol. 54, no. 10, pp. 6076–6090, Oct. 2016.

[11] S. Zhang, J. Li, K. Liu, C. Deng, L. Liu, and A. Plaza, "Hyperspectral unmixing based on local collaborative sparse regression," *IEEE Geosci. Remote Sens. Lett.,* vol. 13, no. 5, pp. 631–635, May 2016.

[12] A. Agathos, J. Li, D. Petcu, and A. Plaza, "Multi-GPU implementation of the minimum volume simplex analysis algorithm for hyperspectral unmixing," *IEEE J. Sel. Topics Appl. Earth Observ.*, vol. 7, no. 6, pp. 2281–2296, Jun. 2014.

[13] I. Dopido, J. Li, P. Gamba, and A. Plaza, "A new hybrid strategy combining semisupervised classification and unmixing of hyperspectral data," *IEEE J. Sel. Topics Appl. Earth Observ.*, vol. 7, no. 8, pp. 3619–3629, Aug. 2014.

[14] L. Zhuang, B. Zhang, L. Gao, J. Li, and A. Plaza, "Normal endmember spectral unmixing method for hyperspectral imagery," *IEEE J. Sel. Topics Appl. Earth Observ.*, vol. 8, no. 6, pp. 2598–2606, Jun. 2015.

[15] J. Li, I. Dópido, P. Gamba, and A. Plaza, "Complementarity of discriminative classifiers and spectral unmixing techniques for the interpretation of hyperspectral images," *IEEE Trans. Geosci. Remote Sens.,* vol. 53, no. 5, pp. 2899–2912, May 2015.

[16] N. Keshava and J. F. Mustard, "Spectral unmixing," *IEEE Signal. Proc. Mag.,* vol. 19, no. 1, pp. 44–57, Jan. 2002.

[17] D. A. Roberts, M. O. Smith, and J. B. Adams, "Green vegetation, nonphotosynthetic vegetation, and soils in AVIRIS data," *Remote Sens. Environ.,* vol. 44, no. 2, pp. 255–269, 1993.

[18] Y. E. Shimabukuro and J. A. Smith, "The least-squares mixing models to generate fraction images derived from remote sensing multispectral data," *IEEE Trans. Geosci. Remote Sens.,* vol. 29, no. 1, pp. 16–20, Jan. 1991.

[19] J. B. Adams, *Imaging Spectroscopy: Interpretation Based On Spectral Mixture Analysis*, C. M. Pieters and P. A. J. Englert, Eds. Cambridge, U.K.: Cambridge Univ. Press, 1993.

[20] J. W. Boardman, F. A. Kruse, and R. O. Green, "Mapping target signatures via partial unmixing of AVIRIS data," in *Proc. Summaries 5th JPL Airborne Earth Sci. Workshop*, 1995, pp. 23–26.

[21] J. Franke, D. A. Roberts, K. Halligan, and G. Menz, "Hierarchical multiple endmember spectral mixture analysis (MESMA) of hyperspectral imagery for urban environments," *Remote Sens. Environ.,* vol. 113, no. 8, pp. 1712–1723, 2009.

[22] M. Theseira, G. Thomas, and C. Sannier, "An evaluation of spectral mixture modelling applied to a semi-arid environment," *Int. J. Remote Sens.,* vol. 23, no. 4, pp. 687–700, 2002.

[23] D. A. Roberts, M. Gardner, R. Church, S. Ustin, G. Scheer, and R. Green, "Mapping chaparral in the santa monica mountains using multiple endmember spectral mixture models," *Remote Sens. Environ.,* vol. 65, no. 3, pp. 267–279, 1998.

[24] J. Li, A. Agathos, D. Zaharie, J. M. Bioucas-Dias, A. Plaza, and X. Li, "Minimum volume simplex analysis: A fast algorithm for linear hyperspectral unmixing," *IEEE Trans. Geosci. Remote Sens.,* vol. 53, no. 9, pp. 5067–5082, Sep. 2015.

[25] Y. Deng and C. Wu, "Development of a class-based multiple endmember spectral mixture analysis (C-MESMA) approach for analyzing urban environments," *Remote Sens.,* vol. 8, no. 4, 2016, Art. no. 349.

[26] T. Liu and X. Yang, "Mapping vegetation in an urban area with stratified classification and multiple endmember spectral mixture analysis," *Remote Sens. Environ.,* vol. 133, pp. 251–264, 2013.

[27] Z. Chen, B. Xu, and B. Devereux, "Urban landscape pattern analysis based on 3D landscape models," *Appl. Geogr.,* vol. 55, pp. 82–91, 2014.

[28] L. Landier, "Modélisation 3D du bilan radiatif des milieux urbains par inversion d'images satellites en cartes de réflectance et de température des matériaux urbains," Université Paul Sabatier-Toulouse III, Toulouse, France, 2018.

[29] L. Landier *et al.*, "3D modeling of radiative transfer and energy balance in urban canopies combined to remote sensing acquisitions," in *Proc. IEEE Int. Geosci. Remote Sens. Symp.*, 2016, pp. 6738–6741.

[30] L. Landier *et al.*, "Calibration of urban canopies albedo and 3D shortwave radiative budget using remote-sensing data and the DART model," *Eur. J. Remote Sens.,* vol. 51, no. 1, pp. 739–753, 2018.
[31] J. Gastellu-Etchegorry *et al.*, "Recent improvements in the dart model for atmosphere, topography, large landscape, chlorophyll fluorescence, satellite image inversion," in *Proc. IEEE Int. Geosci. Remote Sens. Symp.*, 2020*,* pp. 3455–3458.
[32] J.-P. Gastellu-Etchegorry *et al.*, "DART: Recent advances in remote sensing data modeling with atmosphere, polarization, and chlorophyll fluorescence," *IEEE J. Sel. Topics Appl. Earth Observ.*, vol. 10, no. 6, pp. 2640–2649*,* Jun. 2017.
[33] W. Morrison *et al.*, "Atmospheric and emissivity corrections for ground-based thermography using 3D radiative transfer modelling," *Remote Sens. Environ.,* vol. 237, 2020, Art. no. 111524.
[34] J. Gastellu-Etchegorry *et al.*, "Why to model remote sensing measurements in 3D? Recent advances in dart: Atmosphere, topography, large landscape, chlorophyll fluorescence and satellite image inversion," in *Proc. 5th Int. Conf. Adv. Technol. Signal Image Process.*, 2020*,* pp. 1–6.
[35] J.-P. Gastellu-Etchegorry *et al.*, "Simulation of satellite, airborne and terrestrial LiDAR with DART (I): Waveform simulation with quasi-Monte Carlo ray tracing," *Remote Sens. Environ.,* vol. 184, pp. 418–435, 2016.
[36] J.-P. Gastellu-Etchegorry, V. Demarez, V. Pinel, and F. Zagolski, "Modeling radiative transfer in heterogeneous 3-D vegetation canopies," *Remote Sens. Environ.,* vol. 58, no. 2, pp. 131–156, 1996.
[37] Z. Zhen, S. Chen, W. Qin, J. Li, M. Mike, and B. Yang, "A modified transformed soil adjusted vegetation index for cropland in Jilin province, China," *Acta Geologica Sinica,* vol. 93, no. S3, pp. 173–176, 2019.
[38] Z. Zhen *et al.*, "Using the negative soil adjustment factor of soil adjusted vegetation index (SAVI) to resist saturation effects and estimate leaf area index (LAI) in dense vegetation areas," *Sensors,* vol. 21, no. 6, 2021, Art. no. 2115.
[39] L. Landier *et al.*, "Remote sensing studies of urban canopies: 3D radiative transfer modeling," *Sustainable Urbanization; Mustafa Ergen, IntechOpen*, 2016, pp. 227–247.
[40] G. Meister, A. Rothkirch, H. Spitzer, and J. K. Bienlein, "Large-scale bidirectional reflectance model for urban areas," *IEEE Trans. Geosci. Remote Sens.,* vol. 39, no. 9, pp. 1927–1942, Sep. 2001.
[41] F. Gascon, J.-P. Gastellu-Etchegorry, and M.-J. Lefèvre, "Radiative transfer model for simulating high-resolution satellite images," *IEEE Trans. Geosci. Remote Sens.,* vol. 39, no. 9, pp. 1922–1926, Sep. 2001.
[42] Y. Wang and J.-P. Gastellu-Etchegorry, "DART: Improvement of thermal infrared radiative transfer modelling for simulating top of atmosphere radiance," *Remote Sens. Environ.,* vol. 251, 2020, Art. no. 112082.
[43] P. Guillevic and J. Gastellu-Etchegorry, "Modeling BRF and radiation regime of boreal and tropical forest: II. PAR regime," *Remote Sens. Environ.,* vol. 68, no. 3, pp. 317–340, 1999.
[44] J. Li *et al.*, "Analysis of accuracy of MODIS BRDF product (MCD43 C6) based on MISR land surface BRF product-A case study of the central part of northeast asia," *Int. Arch. Photogramm. Remote Sens. Spatial Inf. Sci.,* vol. 42, no. 3, pp. 819–823, 2018.
[45] J. Gastellu-Etchegorry *et al.*, "Modeling BRF and radiation regime of boreal and tropical forests: I. BRF," *Remote Sens. Environ.,* vol. 68, no. 3, pp. 281–316, 1999.
[46] C. Xu, Z. Liu, and G. Hou, "Simulation of the impact of a sensor's PSF on mixed pixel decomposition: 1. Nonuniformity effect," *Remote Sens.,* vol. 8, no. 5, 2016, Art. no. 437.
[47] "SENTINEL-2 products respect stringent radiometric and geometric image quality requirements." 2021. [Online]. Available: https://sentinels.copernicus.eu/web/sentinel/technical-guides/sentinel-2-msi/performance
[48] A. Plyer, E. Colin-Koeniguer, and F. Weissgerber, "A new coregistration algorithm for recent applications on urban SAR images," *IEEE Geosci. Remote Sens.,* vol. 12, no. 11, pp. 2198–2202, Nov. 2015.
[49] G. Brigot, E. Colin-Koeniguer, A. Plyer, and F. Janez, "Adaptation and evaluation of an optical flow method applied to coregistration of forest remote sensing images," *IEEE J. Sel. Topics Appl. Earth Observ.*, vol. 9, no. 7, pp. 2923–2939, Jul. 2016.
[50] A. Saltelli, S. Tarantola, and K.-S. Chan, "A quantitative model-independent method for global sensitivity analysis of model output," *Technometrics,* vol. 41, no. 1, pp. 39–56, 1999.
[51] S. Tarantola, "SimLab 2.2 reference manual," *Inst. Syst., Inform. Saf. Eur. Commission Joint Res. Center*, 2005.
[52] N. Chrysoulakis *et al.*, "Urban energy exchanges monitoring from space," *Sci. Rep.,* vol. 8, no. 1, pp. 1–8, 2018.
[53] C. Feigenwinter *et al.*, "Spatial distribution of sensible and latent heat flux in the city of Basel (Switzerland)," *IEEE J. Sel. Top. Appl. Earth Observ.*, vol. 11, no. 8, pp. 2717–2723, Aug. 2018.
[54] C. Feigenwinter *et al.*, "Spatial distribution of sensible and latent heat flux in the URBANFLUXES case study city basel (Switzerland)," in *Proc. Joint Urban Remote Sens. Event*, 2017*,* pp. 1–4.
[55] T. Cooley *et al.*, "FLAASH, a MODTRAN4-based atmospheric correction algorithm, its application and validation," in *Proc. IEEE Int. Geosci. Remote Sens. Symp.*, 2002*,* pp. 1414–1418.
[56] E. Kalnay *et al.*, "The NCEP/NCAR 40-year reanalysis project," *Bull. Amer. Meteorol. Soc.,* vol. 77, no. 3, pp. 437–472, 1996.
[57] Z. Zhen *et al.*, "Potentials and limits of vegetation indices with BRDF signatures for soil-noise resistance and estimation of leaf area index," *IEEE Trans. Geosci. Remote Sens.,* vol. 58, no. 7, pp. 5092–5108, Jul. 2020.
[58] Z. Malenovský *et al.*, "Variability and uncertainty challenges in scaling imaging spectroscopy retrievals and validations from leaves up to vegetation canopies," *Surv. Geophys.,* vol. 40, no. 3, pp. 631–656, 2019.
[59] G. Meister, W. Lucht, A. Rothkirch, and H. Spitzer, "Large scale multispectral BRDF of an urban area," in *Proc. IEEE Int. Geosci. Remote Sens. Symp.*, 1999*,* pp. 821–823.
[60] P. M. Dare, "Shadow analysis in high-resolution satellite imagery of urban areas," *Photogramm. Eng. Remote Sens.,* vol. 71, no. 2, pp. 169–177, 2005.
[61] R. Welch, "Spatial resolution requirements for urban studies," *Int. J. Remote Sens.,* vol. 3, no. 2, pp. 139–146, 1982.
[62] C. Small, "High spatial resolution spectral mixture analysis of urban reflectance," *Remote Sens. Environ.,* vol. 88, no. 1/2, pp. 170–186, 2003.

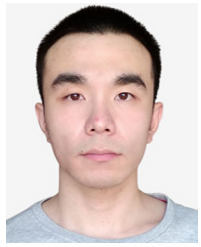

Zhijun Zhen received the B.S. degree in survey and mapping engineering in 2016 from Jilin University, Changchun, China, where he is currently working toward the Ph.D. degree in geographic information system with the College of Geoexploration Science and Technology, in collaboration with CESBIO, Toulouse III University, Toulouse, France.

His research interests include radiative transfer modeling, retrieving, measuring, and analyzing surface bidirectional reflectance distribution function/albedo.

Jean-Philippe Gastellu-Etchegorry (Member, IEEE) received the B.Sc. degree in electricity from ENSEEIHT, Toulouse, France, in 1978, the Aggregation degree in physics from Paris 6 University, Paris, France, in 1981, and the Ph.D. degree in solar physics in 1983 and remote sensing in 1989 from Toulouse III University (UT3), Toulouse, France.

He was with PUSPICS- Remote Sensing Center, Gadjah Mada University, Yogyakarta, Indonesia, and SEAMEO, Bangkok, Thailand, from 1984 to 1990. Then, he was with the Department of Remote Sensing, CESR, Toulouse, France, and CESBIO, Toulouse, France, in 1995. He is currently a Professor with UT3. His research interests include three-dimensional radiative transfer modeling. He has been developing the DART model (https://dart.omp.eu) since 1993.

Shengbo Chen (Member, IEEE) received the Ph.D. degree in earth exploration and information technology from the College of Geoexploration Science and Technology, Jilin University, Changchun, China, in 2000.

He is currently a Professor with the College of Geoexploration Science and Technology, Jilin University, Changchun, China. He has authored more than 200 papers. His research interests include quantitative remote sensing and lunar remote sensing.

Dr. Chen is a member of the IEEE and AGU.

Tiangang Yin received the Ph.D. degree in ocean, atmosphere and continental surface from CESBIO, University of Toulouse, Toulouse, France, in 2015.

He has been extensively involved in the developments of the DART model for the past nine years, especially for LiDAR, atmosphere, and fluorescence modeling. He has been a Research Fellow with the Massachusetts Institute of Technology, Cambridge, MA, USA. He is currently a Research Faculty with the Earth System Science Interdisciplinary Center, Riverdale Park, MD, USA, the University of Maryland, College Park, College Park, MD, USA, and the NASA Goddard Space Flight Center, Greenbelt, MD, USA.

Eric Chavanon received the B.S. degree in computer science from Paris XI (Orsay) University, Paris, France in 1998. After ten years of experience in private companies and two years participation to the end of Planck mission with the Astrophysics Institute of Paris in 2013, since then, he has been a part of the DART project with CESBIO, Toulouse, France.

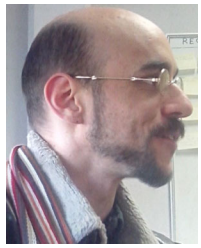

Nicolas Lauret received the master's degree in computer science: digital image engineering from University Toulouse III Paul Sabatier, Toulouse, France, in 2008.

He has been with CESBIO Laboratory in Toulouse, France, as a Developer on the three-dimensional radiative transfer model: DART.

Jordan Guilleux received the master's degree in software development from Paul Sabatier III University, Toulouse, France, in 2014.

He is currently a Software Engineer specialized on GUI and data processing for the DART project with the Centre National de la Recherche Scientifique, Paris, France.